

**Long-range predictability in the tropics**

**Part II: 30-60 day variability**

*Thomas Reichler and John O. Roads*

Scripps Institution of Oceanography

University of California San Diego, 9500 Gilman Dr., La Jolla, CA 92093-0224,

Correspondence to: John O. Roads ([jroads@ucsd.edu](mailto:jroads@ucsd.edu))

Draft from Monday, March 10, 2003

## Table of Contents

Table of Contents .....	2
Abstract .....	3
<b>1. Introduction.....</b>	<b>4</b>
<b>2. Methodology .....</b>	<b>7</b>
a. Experimental design.....	7
b. Analysis method.....	8
<b>3. Simulated and observed intraseasonal variability .....</b>	<b>9</b>
a. Analysis of variance .....	9
b. Wavenumber-frequency spectra.....	10
c. Composite MJO .....	11
<b>4. Predictability of intraseasonal variability.....</b>	<b>12</b>
a. Lead time evolution of total intraseasonal predictability .....	12
b. Interannual variations.....	15
c. Relationship between skill and activity.....	17
<b>5. Phase space representation.....</b>	<b>17</b>
a. Case studies .....	18
b. Predictability of magnitude and phase .....	21
<b>6. Forced intraseasonal variability .....</b>	<b>21</b>
a. Tropical SST variability .....	22
b. Case study .....	23
c. SST-MJO relationship.....	24
<b>7. Summary and conclusion .....</b>	<b>25</b>
References .....	28
Table and Figure Captions .....	33
Table and Figures .....	36

## **Abstract**

The potential predictability of the Madden-Julian oscillation (MJO) and its dependence on initial and boundary conditions was investigated using the NCEP seasonal forecasting model. Five ensemble experiments, forced with different combinations of initial and boundary conditions, were conducted to examine the sensitivity of the simulated MJO to uncertainties in those conditions. By forcing with observed sea surface temperatures (SSTs) the simulated MJO was quite realistic, but the spectral peak was somewhat broad. The initial condition effect on MJO predictability lasted for about 40 days. When model, initial and boundary conditions were all perfect, the useful range of MJO predictability was about 4 weeks, suggesting that the MJO has significant potential to improve long-range predictability. The results were insensitive to ENSO, but predictability was higher when the MJO was more active. Realistic boundary conditions were crucial for good forecast skill, and affected in particular the propagation of the MJO. The boundary forced MJO skill was particularly high during years with large intraseasonal SST activity, which had a synchronizing effect on the phase of the MJO. The consequence from this high sensitivity to boundary conditions is that fully coupled models are needed for further progress in MJO predictability.

## 1. Introduction

The intraseasonal Madden-Julian oscillation (MJO) (e.g. Madden and Julian, 1994) is the dominant mode of tropical low-frequency variability at periodicities between 30 and 60 days. The MJO has predominantly a wavenumber-one structure, which propagates eastward along the equator at about 6 m/s in the Eastern Hemisphere and about 12 m/s in the Western Hemisphere (Waliser et al., 1999b). The slow evolution of the MJO relative to “weather” and its importance for the tropical diabatic heating field suggest that it has the potential to improve long-range predictability (between two weeks and one season). For instance, Winkler et al. (2001) demonstrated with a linear model how consideration of tropical heating, which is associated with the MJO and other effects, can produce predictability as far as seven weeks ahead. Another interesting aspect of the MJO is that it not only impacts the tropics, where the monsoon system or tropical cyclones are affected, but also the extratropics (e.g. Higgins and Mo, 1997).

Although the intraseasonal oscillation may have the potential to improve long-range predictability, its practical realization is hampered by several factors. First, the MJO is not well understood, although several physical mechanisms have been proposed to explain it. Furthermore, cumulus convection, which is a key aspect of the MJO, is only crudely represented in current models. The consequence is that models often have problems in simulating an adequate MJO (e.g., Slingo et al., 1996). The MJO is also difficult to predict because it is a very irregular occurring phenomenon, suggesting that its nature is chaotic and essentially unpredictable. Additional complications arise from large errors, which are contained in tropical analysis. They are related to the sparse observational

network, and the lack of direct observations of divergence and diabatic heating, which are important for the simulation of the MJO (Hendon et al., 2000).

Relatively few studies have examined the forecast skill of the MJO with dynamical models. Chen and Alpert (1990) investigated the predictability of the oscillation with the medium range forecast (MRF) model, and found from filtered upper level velocity potential that the useful limit is reached at about 8 days. Very similar predictability ranges were found by Lau and Chang (1992), Boer (1995), and Jones et al. (2000). The relatively short range of 8 days did not really offer much hope for improving long-range predictability. This short forecasting time was also somewhat surprising when considering the time scale of the MJO and the intuitive notion that predictability for a given process should be approximately proportional to its life time (van den Dool and Saha, 1990).

Previous predictability studies had two important things in common: First, forecasts were verified against observational data. Well known model deficiencies led to a dramatic decrease in predictability. Second, predictability was understood as a pure initial condition problem, but uncertainties in tropical analysis introduced errors into the forecasts. In addition, the possible role of boundary forcing for the MJO was largely neglected. The DERF experiments from the National Centers for Environmental Predictions (NCEP), for example, used sea surface temperature (SSTs), which were damped to climatology from observed initial states with an e-folding time of 90 days (Schemm et al., 1996). It is, however, getting clearer that in addition to atmospheric internal dynamic instability, thermodynamic processes from the ocean interacting with the atmosphere are important in sustaining the MJO (e.g., Flatau et al., 1997; Waliser et al., 1999a). Very recently, Schubert and Wu (2001) and Wu et al. (2002) found from ensemble simulations from 10

different atmospheric general circulation models (AGCMs) that prescribing observed weekly SSTs as boundary conditions led to significant MJO-like responses.

To avoid the problems of previous studies, we asked what the inherent predictability properties of the MJO would be if model, initial and boundary conditions would be almost perfect. That is, we used a perfect model approach (e.g. Buizza, 1997), where one forecast was verified against another forecast with the same model. If the MJO is essentially chaotic and sensitively dependant upon initial condition perturbations, what is the time scale of predictability under perfect conditions, and how does it compare to real world forecasts? This research was also aimed at understanding how sensitive the simulated MJO was to uncertainties in initial and boundary conditions. In a companion paper (Reichler and Roads, 2003b), we investigated the predictability of monthly means in the tropics. The main difference between these two studies is variability on interannual time scales, which is contained in monthly means, but which has been eliminated in this study. For monthly means, boundary conditions are the main contributor to predictability. However, it was also found that even these longer-range forecasts were sensitive to initial conditions for many weeks. For forecasts of intraseasonal variability, good initial conditions are of course crucial, but how sensitive are MJO simulations to boundary conditions? This question is of practical importance since operational forecasts use SST boundary conditions which may contain large errors, either because simple methods like climatological or persisted SSTs are used, or because of the limitations of the ocean model.

The paper is structured as follows: Methodological aspects are discussed in section 2. The character of the simulated intraseasonal variability is described in section 3. Section 4 describes the intraseasonal predictability for the different experiments. In section 5, the

predictability of the MJO is described both for its propagation and as well as for its strength. In section 6, the forced component of intraseasonal variability and its relationship to SSTs is examined further. Summary and conclusions are presented in section 7.

## **2. Methodology**

### *a. Experimental design*

This study is based on the NCEP seasonal forecasting model (Kanamitsu et al., 2002; Reichler and Roads, 2003a,b) using T42 resolution and 28 vertical levels. The model was used to conduct predictability experiments with 10-20 individual ensemble members. Five experiments were run, as summarized in Table 1 and described in detail in the following paragraphs.

All experiments were performed globally, although the focus of this study was on the tropics. Forecasts were initialized at December 15<sup>th</sup> and run continuously for 14 weeks until the end of the following March. Each experiment was repeated for 22 northern hemispheric winter seasons from 1979 to 2000. Individual simulations for each experiment, year and season were forced with identical boundary conditions, but were started from slightly different initial conditions. They were taken from special base runs or from reanalysis, which were perturbed using the breeding technique (Toth and Kalnay, 1993). Details about the specific implementation of the breeding method are described in Reichler and Roads (2003a). The two continuous base runs were “BASE-O”, which was forced with observed SSTs and sea ice, and “BASE-C”, which was forced with climatological SSTs and sea ice.

Experiments are designated by specific acronyms, which indicate the type of initial and boundary conditions (Table 1). Three experiments were forced with observed ocean

boundary conditions (SSTs and sea ice), but started from different initial conditions. The perfect experiment “ICBC” was initialized from “anomalous” initial conditions (BASE-O), which is equivalent to using observed initial conditions under the perfect model assumption; “BC” was started from randomly chosen “climatological” initial conditions (BASE-C); “iBC” was started from initial conditions by integrating ICBC for one whole year. The motivation for iBC was to find out how much predictability might be lost by excluding the beneficial effects of synoptic scales in the initial conditions. These initial conditions have completely lost their memory from the previous year, but they are adjusted to the boundary forcing at the new initialization time. The second group of experiments started from perfect initial conditions, but was forced with imperfect boundary conditions: “IC” was forced with climatological boundary condition, and “ICP” was forced with persisted ocean boundary conditions, which is a common alternative to more expensive dynamical ocean forecasts (e.g., Mason et al., 1999; Roads et al., 2001).

#### *b. Analysis method*

We used as a basic measure of MJO activity the 200 hPa velocity potential averaged from 10°N to 10°S ( $\chi_{200}$ ). This quantity represents large-scale aspects of the divergent flow at the approximate level of maximum outflow of deep convective systems. Before analyzing the data, they were filtered in the following way: The daily climatological mean annual cycle from the corresponding experiment was first removed. We refer to these anomalies as unfiltered data. Next, the data were filtered in time with a 30-70 day band pass filter, using an iterative moving average procedure similar to that described by Waliser et al. (1999b). The filtering was performed separately for each 107 day long forecast at each grid point over all ensemble members and years.



Variability of  $\chi_{200}$  was analyzed by separating it into an externally forced component (signal) and into internally generated noise. Following the approach of Rowell (1995), the signal was calculated from the variability between ensemble means (intraensemble variance) and the noise from the variability between individual members around the ensemble mean (interensemble variance). Predictability of  $\chi_{200}$  was measured in terms of the spatial anomaly correlation (AC) over the equatorial domain between a *prediction* and a *verification* data set. As prediction data, 10-member ensemble means of the experiment under consideration were used. To determine “real world” skill, reanalysis was used as verification data. In most cases, however, the “perfect world” skill was calculated by using single realizations of the perfect experiment ICBC as verification. Each of the 20 members of ICBC was selected as verification, and the average was used as the final estimate of predictability. Since AC values are bounded by  $\pm 1$ , we applied a Fisher Z transformation (e.g., Roads, 1988) before adding or subtracting them, and then again transformed back to normal correlations.

### 3. Simulated and observed intraseasonal variability

In a companion paper (Reichler and Roads, 2003b) the general performance of the model in the tropics was discussed in terms of its climatology and interannual variability. It was found that key-variables for tropical circulation compared well with observations. In this section, we assess the ability of the model to simulate the MJO to provide a context for the subsequent results which were based primarily on model data.

#### *a. Analysis of variance*

Fig. 1a presents the spatial distribution of total intraseasonal variability from simulations ICBC and IC in comparison to NCEP/NCAR reanalysis. Variances were

calculated from daily intraseasonally filtered  $\chi_{200}$  at lead times between 41 and 106 days, as described in the previous section. The first 40 days were excluded to avoid the deterministic predictability period which was influenced by initial conditions. The variance of the model was very similar to reanalysis in both magnitude and spatial distribution. Both indicate typical activity maximum over the Indian Ocean, and fewer activity over the Pacific Ocean. There was also increased activity over the Atlantic Ocean, which was more pronounced in the simulations than in the reanalysis. The main difference was that the simulated variance was somewhat larger than the observed one. Another difference was that the reanalysis exhibited one relatively broad center of activity over the Indian Ocean, whereas the simulations had two maxima. Simulation IC also had less variability than ICBC, indicating that boundary forcing increased total intraseasonal variability.

The ratio of external to internal intraseasonal variability for simulation ICBC and IC is shown in Fig. 1b. As expected from the climatological boundary forcing, simulation IC had no forced variability. Simulation ICBC, on the other hand, exhibited a signal to noise ratio of about 0.1. This value is relatively small compared to signal to noise ratios of 0.2-0.3 that were found by Wu et al. (2002) from 10 different AGCMs over two full years. This demonstrated clearly that boundary forcing did affect intraseasonal variability, but also that this effect was rather small. The forced variability was higher over the Indian Ocean region, which coincides with the region of increased convective activity.

#### *b. Wavenumber-frequency spectra*

Fig. 2 shows wavenumber-frequency spectra of  $\chi_{200}$  for NCEP/NCAR reanalysis, as well as for experiments ICBC and IC. The spectra were calculated from daily fields, individually for each members and year. The final results shown in Fig. 2 are averages

over all years and members. In the reanalysis (Fig. 2a), the eastward propagating wavenumber one was the largest component. It had a broad spectral peak centered at 54 day period, which is traditionally attributed to the MJO phenomenon. The secondary maximum at zero frequency corresponds to the seasonal mean, since interannual variability was not removed from the data. The spectrum from the perfect experiment ICBC (Fig. 2b) showed less concentration of energy on a single wavenumber as the reanalysis. Nevertheless, most energy was in the eastward going wavenumber-one component, and there was a secondary peak at about the same period as reanalysis. The spectrum for simulation IC (Fig. 2c) contained less energy than ICBC at the very low frequencies. This was mainly a consequence of using climatological instead of observed SSTs, which eliminated most of the interannual variability. The spectral peak of IC at 36 days was at a higher frequency than observed, which is a typical problem for many AGCMs (e.g., Hayashi and Golder, 1993; Kuma, 1994; Slingo et al., 1996). It is interesting, however, that the forcing with observed SSTs reduced somewhat this problem, as the spectrum from simulation ICBC demonstrates. This indicates that the MJO of this model was sensitive to boundary forcing.

### *c. Composite MJO*

Further characteristics of the MJO in reanalysis and model can be gathered from the time-longitude representation of composite events (Fig. 3). The composites were calculated by averaging over the  $n$  strongest MJO events based on the value of filtered  $\chi_{200}$  at 150°E. Taking into account the different ensemble size of the data sets,  $n$  was 20 for reanalysis, 200 for ICBC, and 100 for IC. The strength of the MJO for reanalysis and simulations was very similar, but the activity in the simulations tended to be spatially more

localized than in the reanalysis. The composites allowed an estimate of the average periodicity of the MJO. It was about 41 days for reanalysis, 40 days for ICBC, and 31 days for IC, which again indicated that the use of observed SST forcing leads to more realistic simulations of the MJO.

Overall, these results demonstrated that the model was able to simulate a reasonable MJO when it was forced with observed SSTs. The model shows a clear eastward propagating signal with reasonable strength and periodicity. The main shortcoming was that the model was not able to simulate the dominance of the intraseasonal oscillation at periods of 50 days. It simulates too much power at higher frequencies, in particular when it was forced with climatological SSTs, again which is typical of many AGCMs.

#### **4. Predictability of intraseasonal variability**

##### *a. Lead time evolution of total intraseasonal predictability*

In this section, we describe the perfect model predictability of the MJO and its sensitivity to initial and boundary conditions. This was accomplished by examining the spatial anomaly correlation (AC) for the various experiments as a function of lead time. Daily fields of intraseasonally filtered  $\chi_{200}$  were used for the AC calculation. Fig. 4 shows the evolution of the ACs from initialization (Dec. 15<sup>th</sup>) out to day 106 (March 31<sup>st</sup>) for the five experiments.

Fig. 4a shows ACs averaged over all 22 years (1979-2000) years. Simulation ICBC, verified against itself (continuous line), provides the upper predictability limit of the MJO. Model, initial and boundary conditions were all perfect, except for small perturbations in the initial conditions. These perturbations grew through non-linear chaotic interactions and

led to divergence of the various forecasts. The curve for ICBC shows the classical loss in predictability with forecast range. If a correlation of 0.4 is taken as the minimum for useful skill, then the limit of MJO predictability is reached at about 4 weeks. This range was much longer than the 8 day limit found from previous studies. The main reason for this difference are not due only to the perfect conditions for experiment ICBC, but also because some other methodological differences like meridional and ensemble averaging. After 30-40 days or so, deterministic predictability of ICBC was completely lost, and the skill reached a constant value of about 0.2. This small but nevertheless non-zero skill is due to the effects of boundary forcing on intraseasonal variability. Simulations iBC and BC, which started from imperfect initial conditions, but which were forced with the same perfect boundary conditions, showed similar correlations at this long lead. This result confirms the non-zero signal to noise ratio, which was found in the previous section from simulation ICBC.

The range of useful predictability for ICP (dashed-dotted curve), as measured by a correlation of 0.4, extended to about three weeks. This was roughly one week less as compared to having perfect boundary conditions, but it was still much longer than 8 days reported from previous studies. ICP reached zero skill at about 40 days, indicating that the effects of forced and initial condition predictability were both zero at this time. The skill of experiment IC, which was forced with climatological initial conditions, decayed even faster. This was presumably due to the adjustment of the atmosphere to climatological boundary conditions and its impact on the MJO. The useful limit was reached after only 9 days, and zero skill was reached at about 30 days. The differences in predictability between ICBC and ICP, and between ICBC and IC showed very clear that the simulation of the

MJO was sensitive to boundary forcing. Overall, these results indicate that air-sea interaction is potentially important for the simulation of the MJO.

We were also interested in finding out whether strong boundary forcing from the El Niño Southern Oscillation (ENSO) phenomenon affected the predictability of the MJO. In the past, the demonstration of a connection between ENSO and MJO has been somewhat controversial. Some studies suggested that the activity of the MJO was controlled by ENSO (e.g., Gutzler, 1991; Fink and Speth, 1997), while others found little evidence for such a link (e.g., Slingo et al., 1999; Hendon et al., 1999). We repeated the calculation of the ACs by averaging only over weak-to-neutral ENSO years. Strong cold and warm ENSO years during the 1979-2000 period were 1983, 1985, 1987, 1989, 1992, 1998, 1999 and 2000; neutral-to-weak ENSO years were all the other years. Fig. 4b shows the average evolution of predictability during those years. Since fewer years were included in the average, the curves were somewhat noisier than before. However, the ACs of the various experiments were very similar to using all years, and showed no evidence that the state of ENSO might have had any effects on the predictability of the MJO.

We also examined the predictability of simulations ICBC-r and IC-r verified against reanalysis. The comparison between ICBC-r and ICBC gives an estimate of how strong the model related error component is. Fig. 5a shows forecast skill computed from  $\chi_{200}$ . The unsmoothed results for ICBC-r and IC-r (thin curves) are very noisy, since only one realization (the real atmosphere) was used as verification. Therefore, it is better to study the smoothed (thick) curves instead. To the extent that the smoothed results were representative, the skill of ICBC-r was very similar to that of ICBC. This is somewhat surprising, and means that model related errors are not very large. This may be related to

the fact that the divergent circulation is not an observed quantity. Therefore, velocity potential may be strongly influenced by the assimilation model of the reanalysis, which may have similar biases as the AGCM of this study. We therefore repeated the calculations of predictability by replacing  $\chi_{200}$  with zonal winds at 200 hPa ( $u_{200}$ ). Since winds are observed, they should be closer to real observations in the reanalysis. Fig. 5b shows the results for  $u_{200}$  from ICBC-r and ICBC, each verified against itself. For ICBC, the predictability of  $u_{200}$  was very similar to that of  $\chi_{200}$ , at all lead times. The difference between ICBC-r and ICBC shows that model related errors are now more important. The limit of useful skill for ICBC-r was reached at about 20 days, whereas that for ICBC extended out to 27 days. Also the purely forced part of predictability at long lead times was lower for ICBC-r than for ICBC.

*b. Interannual variations*

Fig. 6 presents a year by year breakdown of intraseasonal predictability. This breakdown allowed us to identify years where predictability was particularly high or low, and to find out how important initial and boundary conditions were during those years. As before, we analyzed the intraseasonal anomalies over some lead time interval during individual years, measured from filtered  $\chi_{200}$ . As discussed before, the effects of initial conditions on intraseasonal predictability lasted on average for about 40 days. Consequently, predictability was analyzed separately for a short lead time interval (day 0-40), where deterministic predictability from perfect initial conditions was high, and a long lead time interval (day 41-106), where the initial condition effect was small and the forced variability of the MJO was important.

Fig. 6a presents the average ACs during the short lead time interval for the three experiments ICBC, IC, and ICP, which were started from perfect initial conditions. The perfect experiment ICBC (black bars) exhibits a rather large interannual variability in predictability, implying a possible dependence on the particular flow state. During some years (e.g., '88, '96), the forecast skill from initial conditions alone (simulation IC, green bars) was surprisingly close to that of ICBC. This indicates that the MJO was a very robust feature during those years. During other years (e.g., '83, '89, '93), however, simulation IC shows much smaller skill than ICBC, indicating that the MJO can be very sensitive to additional uncertainties introduced by boundary forcing. The correlations for experiment ICP (blue bars) usually followed very closely those of ICBC, which suggests that the results were very robust and reproducible. On the other hand, correlations from ICP were also consistently smaller than ICBC, indicating how important boundary forcing for the MJO was.

The year to year variations in predictability for the long lead time interval (day 49-106) are shown in Fig. 6b. Only the results for experiments ICBC, iBC and BC are presented, since they were forced with perfect boundary conditions. At this long lead time interval, predictability resulted only from the forced intraseasonal response. As expected, the skill of ICBC was generally lower than at the short lead time interval. However, there were some years (e.g., '90, '92) during which the ACs were remarkably high. Results for BC and iBC followed closely those of ICBC, which was consistent with the common effects of boundary forcing.



### *c. Relationship between skill and activity*

The relationship between forecast skill and the activity of the intraseasonal oscillation is somewhat controversial. Some previous studies found that forecast skill increased when the MJO was more active (Ferranti et al., 1990; Lau and Chang, 1992), whereas others found the opposite (Chen et al., 1993), or no relationship (Boer, 1995). We examined this relationship for experiment ICBC. Fig. 7 shows for individual years the spatio-temporal variance of bandpass filtered  $\chi_{200}$ . Variance was calculated in space along the equator and in time from forecast day 0-40 (a) and 41-106 (b). There exists a modestly good relationship between year to year variations of predictability and activity, as can be seen by comparing with Fig. 6. The correlation for the short lead time interval was 0.6, and for the long lead time interval 0.48. Both correlations were statistically significant at the 95% error level.

## **5. Phase space representation**

In the following, the MJO is investigated in Fourier space in terms of the complex expansion coefficients of the wavenumber one component. From the spectral energy distribution presented before it is clear that most of the intraseasonal energy of  $\chi_{200}$  was contained in this wavenumber. In fact, wavenumber one was often taken as the defining parameter for studies of the MJO (e.g., Lorenc, 1984; Slingo and Madden, 1991; Boer, 1995). The advantage from the spectral representation is that the spatial  $\chi_{200}$  field is represented by just two real variables, the phase and magnitude of its wavenumber one component. The phase represents the propagation of the intraseasonal oscillation, and the magnitude its strength or activity. The idea behind this approach is somewhat similar to the decomposition into two eigenmodes, which was more widely used in previous MJO studies

(e.g., Lorenc, 1984; Chen and Alpert, 1990; Ferranti et al., 1990; Jones et al., 2000). The Fourier decomposition of intraseasonally filtered  $\chi_{200}$  in the east-west direction along the equator is defined by

$$\chi_{200}(\lambda, t) = \sum_{m=-N}^N z_m(t) e^{im\lambda}, \quad (1)$$

where  $z_m$  are complex Fourier expansion coefficients and  $m$  the wavenumber. The complex wavenumber one coefficient can be also written in polar coordinates,

$$z_1 = r \exp(i\varphi). \quad (2)$$

Then, the magnitude  $r$  represents the strength of the oscillation, and the phase  $\varphi$  the propagation. From the magnitudes, anomalies with respect to the 1979-2000 climatology were calculated. When correlations are calculated, the  $2\pi$ -periodicity of the phases would lead to problems. This was avoided by representing the phase angles by

$$\Phi = \sin(\varphi). \quad (3)$$

Note that this definition could lead to some ambiguity because of the cyclic nature of the sine function.

#### *a. Case studies*

Phases and magnitudes of the MJO during 1992 are examined here in more detail. From the annual breakdown of predictability it is known that during 1992 the forecast skill of experiment ICBC was moderately high for the short (0.6 correlation), and unusually high for the long (0.55 correlation) lead time interval. Fig. 8 presents for the five experiments the evolution of filtered  $\chi_{200}$  in terms of wavenumber-one magnitude and phase. Each panel shows the evolution of  $\chi_{200}$  from individual members (thin lines) as well as ensemble means (thick lines). The ensemble means show variability which is common

to all members, either because of the initial condition memory, or because of the effects of boundary forcing. From the spread of individual members around the mean one can estimate how certain an individual forecast was.

The phases  $\Phi$  for the five experiments are shown in the left panels of Fig. 8. At short leads, phases of individual members of ICBC, IC and ICP tended to be similar because of the initial condition effect. The phases of experiments iBC and BC, which started from different initial conditions than ICBC, were less coherent, and did not agree well with ICBC. Out to very long lead times, individual members of IC showed a relatively high degree of coherence, even so they were forced with climatological SSTs. This can also be seen from the regular oscillations of the ensemble mean. During the 107 day long simulation there was an approximate passage of 3.5 MJO cycles, corresponding to a mean period of about 30 days. Experiments with observed SSTs had a longer periodicity. This has already been noted in the previous discussion of the spectra. The spread for experiment ICP was very large, in particular after day 30. Experiment ICBC indicated additional interesting behavior. At forecast day 30 or so, the phases transitioned into a different cycle. After that, individual members were again in very good agreement. At the same time, the phases of iBC and BC also agreed well with ICBC, in particular during forecast days 40-80. As we will show later, this synchronizing effect was related to strong intraseasonal SST activity during that time. The right panels of Fig. 8 present the evolution of the magnitude anomalies  $r$ . Magnitudes had less coherence than the phases. The ensemble means varied close around zero, which corresponds to the climatological mean. Only experiments ICBC, iBC and BC exhibited some increased activity during the second half of the forecast.

Let us now focus on the ensemble mean response. In this case, a phase space representation is advantageous, because it allows the combination of magnitude and phase in a single graph. Consider first the situation for 1992 (Fig. 9a). Shown is the evolution of the wavenumber-one Fourier coefficient of filtered  $\chi_{200}$  in the complex plane, where the magnitude  $r$  is represented by the distance to the origin, and the phase  $\varphi$  by the angle from the positive x-axis. Time is indicated by different colors. The similarity between trajectories of individual experiments is a measure of predictability. At short lead times (0-20 days, red and orange colors), the trajectories of ICBC, IC, and ICP were quite similar. After that, experiment IC had continuous regular oscillations but the magnitude decreased because of the gradual decorrelation of individual members. The trajectory of ICP was very distorted at longer lead times (green and blue colors), since the coherence between members was lost. Experiment ICBC exhibited the already mentioned regime shift at about day 30 (yellow color), and then continued with regular oscillations. After the shift, the trajectories of iBC and BC were very similar in phase as well as in magnitude to ICBC, owing to the strong forced variability in all three experiments.

As another example, Fig. 9b presents the MJO evolution during 1996. From Fig. 6 one can see that during this year initial condition (0.5 correlation) as well as boundary forced predictability (0.4 correlation) was modestly high. Similar as before, the trajectories of ICBC, IC and ICP agreed well at short leads (red colors). At longer leads, IC continuous to oscillated quite regularly and performed about 3.5 oscillations. As before, simulation ICBC exhibited a regime shift at about day 20 (yellow color), and at longer leads (greenish and bluish colors), the trajectories of ICBC, iBC and BC were quite similar.

### *b. Predictability of magnitude and phase*

Fig. 10 presents predictability of magnitudes  $r$  (a.) and phases  $\Phi$  (b.) as a function of lead time. Predictability at a certain lead time was measured from the temporal correlation between a prediction and a verification time series, which consisted of the year to year variations in  $r$  or  $\Phi$  at this lead. As before, 10 members ensemble means of the corresponding experiment were used as prediction data, and individual members of simulation ICBC were used as verification data. The overall lead time evolution of predictability for  $r$  and  $\Phi$  was similar to that of total predictability (Fig. 4). Boundary forcing, for example, led to non-zero forecast skill at long lead times for both  $r$  and  $\Phi$ , as can be seen from the results for experiments ICBC, iBC, and BC.  $r$  and  $\Phi$  had characteristic differences in terms of their predictability. Phases were generally better predictable than magnitudes. In other words, the propagation of the intraseasonal oscillation was better predictable than its strength. This may be related to the slow propagation of the intraseasonal oscillation, which causes a high degree of persistence in its phase. Simulation ICP reveals another interesting phenomenon: Uncertainties associated with the use of persisted ocean boundary conditions impacted mostly the phase of the MJO. This indicates that the propagation speed of the intraseasonal oscillation was particularly sensitive to boundary forcing.

## **6. Forced intraseasonal variability**

In this section, the relationship between SST forcing and intraseasonal variability is examined in more depth. It was shown before that boundary forcing affected intraseasonal activity, and that it led to long lead predictability with an average correlation of 0.2. However, there were considerable year to year variations, and during certain years, the

forced variability could be strong and important for predictability. The previous analysis showed that for example 1990, 1992, 1996 and 2000 were such years. Therefore, most of the following analysis was focused on those years.

*a. Tropical SST variability*

SST patterns with a similar spatio-temporal structure as the MJO are very effective in forcing atmospheric intraseasonal variability, much in the sense of resonant forcing of a dynamical system. From observational studies it is known that tropical SSTs have an intraseasonal peak (e.g., Krishnamurti et al., 1988). This peak is coherent with observed changes in surface heat fluxes and SSTs that occur during the passage of an MJO (e.g., Zhang, 1996; Flatau et al., 1997; Maloney and Kiehl, 2002). Local SST variations in association with the passage of an MJO can reach  $1.0^{\circ}\text{C}$  and more (Weller and Anderson, 1996). We investigated space-time spectra of the SSTs seen by experiment ICBC to find out whether there were any links to predictability. Before the spectra were computed, the annual mean as well as the annual and semi-annual seasonal cycle were removed from the SST data. In space, spectra were calculated along the equator. This was repeated for all latitudes between  $10^{\circ}\text{N}$  and  $10^{\circ}\text{S}$ , and the final results were averaged over those latitudes. Fig. 11 presents for each year the amount of SST energy in the 54 day band. Shown are averages for the eastward traveling wavenumbers 0-3. Clearly, 1992 contained the maximum energy of all years. The comparison with Fig. 7b shows that long-lead intraseasonal predictability was usually higher during years with larger intraseasonal SST energy. The correlation between both quantities was 0.58. This was relatively high, in particular when considering that such a relationship was not necessarily linear, and that other factors beside SST forcing determined predictability as well.

*b. Case study*

Next, the situation for 1992 was studied in more detail. Fig. 12 presents a one by one comparison of tropical SST anomalies and associated intraseasonal activity from reanalysis (a) and simulation ICBC (b). The SSTs, which are shown by shading, are identical in both panels and represent latitudinal averages from 10°N to 10°S. The SSTs exhibited the typical signature of an ENSO warm event, with warmer waters over the Pacific, and colder waters over the warm pool region. Superimposed on this mean pattern is strong intraseasonal SST variability. The overlaid black contour lines show the evolution of the MJO as given by filtered  $\chi_{200}$ . The reanalysis (Fig. 12a) exhibited a good relationship between SST anomalies and MJO activity. SSTs were warmer before the period of active convection (negative  $\chi_{200}$ ) and cooler after it. Simulation ICBC (Fig. 12b) showed also a clear MJO signal, which seemed to be shifted by about 1 quarter cycle towards earlier times with respect to the reanalysis. This led to a more direct relationship between SST and MJO activity, in the sense that anomalous rising motions tended to coincide directly with warm or neutral SST anomalies, and sinking motions with cold SST anomalies. This good relationship suggest that SST forcing with proper frequencies can phase lock the simulated MJO into its own cycle.

The intraseasonal SST variations over the warm pool region amount only to 0.6°C or so. It is interesting that such small variations in temperature could control the intraseasonal activity in the model. To explain this behavior it is important to understand that the atmospheric response to tropical SSTs is strongly non-linear. Observations show that SSTs above 26-27°C are required for large-scale deep convection to occur, and that little convective activity takes place over SSTs colder than that (e.g., Graham and Barnett,

1987). Since the mean SSTs over the Indian Ocean during January were close to the 27°C threshold, even small anomalies were effective in controlling convective activity.

*c. SST-MJO relationship*

A more general relationship between SST and MJO is derived from composites of many MJO events. The contours in Fig. 13 show composites of strong MJO events for simulation ICBC (top panels) and for reanalysis (bottom panels). Similar as in Fig. 3, the composites were formed by selecting the  $n$  strongest MJO events from intraseasonally filtered data over a specific base point. Two different base points, one over the Indian Ocean (90°E) and one over the warm pool (150°E), were selected to capture different stages of the MJO. The SSTs are shown by shading. As shown in all four panels, the SSTs exhibited strong intraseasonal variability, even though data were unfiltered. This indicates again that intraseasonal SST variability was associated with similar variability in the atmosphere. The SSTs for the reanalysis had more noise than the simulation because of the smaller sample size. In the model (top panels), convection was again enhanced (suppressed) by warm (cold) SST anomalies almost directly underneath. In the reanalysis (bottom panels), the regions of warmest SST anomalies tended to lead the convective anomalies by several days.

To better quantify the relationship between MJO and SST, cross-correlations between the composite MJO and associated SST anomalies were calculated for different phase lags (Fig. 14). Temporal correlations were computed between the filtered  $\chi_{200}$  time series at a fixed grid point and SST anomaly time series at different positions to the east or west of the point. Results from all grid points along the equator were averaged. For the reanalysis (continuous lines), the MJO had the strongest negative correlations with SSTs at



a phase lag of about  $60^{\circ}\text{E}$  or about 7 days. The two different base points lead to very similar results. The correlations are negative since cool (negative) SST anomalies tend to suppress convection, which leads to positive velocity potential anomalies (upper level convergence). The  $60^{\circ}$  phase shift agrees well with the general picture seen before: SSTs are higher before the period of active convection and lower after it. This is also in line with observational findings from Flatau et al. (1997), which showed that to the east of the area of active convection, in the convergence region of a Kelvin wave, increased downward fluxes of shortwave radiation in conjunction with mostly cloud free conditions generated positive SST anomalies. In the vicinity of enhanced convection, cloud shielding and strong air-sea sensible and latent heat fluxes cooled the local SSTs. To the west of the convection, enhanced latent heat fluxes associated with increased surface westerlies tended to further cool the SSTs. For simulation ICBC (dashed lines), maximum negative correlations occurred for SST anomalies at phase lags of only about  $10^{\circ}\text{E}$ . This much smaller eastward shift reflects the different MJO-SST relationship between model and nature. In nature, SST variations are caused by the MJO as outlined above. In the model, however, prescribed SSTs force the atmosphere above, so that the simulated MJO tends to be almost in phase with the SST. These results are also in line with Wu et al. (2002), who found that simulated and observed velocity potential anomalies tend to be in quadrature with the simulations leading the observed anomalies by about 10 days.

## **7. Summary and conclusion**

This study investigated the predictability of tropical intraseasonal oscillations and their sensitivity to initial conditions and boundary forcing. Five AGCM experiments were conducted with the NCEP seasonal forecasting model, each with different combinations of

initial and boundary conditions. Most results were based on intraseasonally filtered 200 hPa velocity potential in the tropics. When forced with observed weekly SSTs, the model exhibited a intraseasonal signal-to-noise ratio of about 0.1, showing that some variability was due to thermodynamic forcing from the ocean. The simulated MJO was quite realistic, with a clear eastward propagating signal, reasonable strength and periodicity. When climatological instead of observed SSTs were used, the spectral peak of the simulated MJO shifted toward higher frequencies. This problem is typical for many AGCMs, and indicated that the model's MJO is sensitive to boundary forcing. The upper limit of MJO predictability with perfect model, initial and boundary conditions averaged out to 28 days. This relatively long time scale suggests that good forecasts of the MJO have the potential to improve long-range predictability.

The initial loss of predictability for the MJO is much slower than for classical predictability of extratropical weather, and the initial condition effect on the MJO lasted for about 40 days. After this period, forcing with observed SSTs still produced some skill, as was to be expected from the non-zero signal-to-noise ratio. Boundary forcing was very important for good simulations of the MJO. When using persisted instead of observed SSTs, the range of useful predictability was reduced to about 23 days, and with climatological SSTs it was less than 10 days. During some years, initial conditions alone led to very robust MJO simulations, while in other years, boundary conditions were more important for good predictability. The activity of the MJO was one factor which led to these interannual variations, in the sense that predictability was higher when the MJO was more active. There was no evidence that ENSO forcing might affect the predictability of the MJO.

Phase and amplitude of the wavenumber-one component were used to investigate predictability of the MJO separately for its propagation and strength. During some years, boundary forcing strongly influenced the propagation of the MJO. Spectral analysis of observed tropical SSTs revealed a positive relationship between frequency of the SST forcing and intraseasonal predictability. During years where the SST energy in the intraseasonal band was high, the forced intraseasonal response of the atmosphere was high, and so was predictability. A case study demonstrated that prescribed SST variations with strong intraseasonal energy can phase lock the MJO into a cycle similar to the observations. The general relationship between MJO and SST in nature and in the model was investigated from composites of many MJO events. In nature, MJO activity tends to drive intraseasonal SST anomalies, so that SSTs are higher before the period of active convection and lower after it. In the model, where SST anomalies force intraseasonal variability, MJO and SST tend to be more in phase, with enhanced convection almost directly above positive SST anomalies.

This study gave clear evidence that the MJO has the potential to improve long-term predictability if good initial and boundary conditions can be obtained. Consistent with other studies (e.g., Wu et al., 2002) it was found that boundary forcing is a controlling element for the MJO, and that boundary forcing mostly influences the propagation of the MJO. The forced predictability, which was found from prescribing weekly SST observations, does of course not imply the same predictability under real conditions. The problem is that SSTs themselves are to some extent the product of the unknown atmospheric forcing. Real predictability with prescribed SSTs is only given to the extent that the atmosphere is sensitive to preexisting SST anomalies, for example from previous

MJO events. The coupled nature of the MJO requires boundary conditions, which can evolve and interact with the atmosphere in time. Further progress in long-range predictability will be achieved with fully coupled models.

## References

- Boer, G. J., 1995: Analyzed and Forecast Large-Scale Tropical Divergent Flow. *Mon Weather Rev*, **123**, 3539-3553.
- Buizza, R., 1997: Potential forecast skill of ensemble prediction and spread and skill distributions of the ECMWF ensemble prediction system. *Mon Weather Rev*, **125**, 99-119.
- Chen, S. C., J. O. Roads, and J. C. Alpert, 1993: Variability and Predictability in an Empirically Forced Global Model. *J Atmos Sci*, **50**, 443-463.
- Chen, T. C. and J. C. Alpert, 1990: Systematic Errors in the Annual and Intraseasonal Variations of the Planetary-Scale Divergent Circulation in NMC Medium-Range Forecasts. *Mon Weather Rev*, **118**, 2607-2623.
- Ferranti, L., T. N. Palmer, F. Molteni, and K. Klinker, 1990: Tropical–extratropical interaction associated with the 30–60 day oscillation and its impact on medium and extended range prediction. *J Atmos Sci*, **47**, 2177–2199.
- Fink, A. and P. Speth, 1997: Some potential forcing mechanisms of the year-to-year variability of the tropical convection and its intraseasonal (25-70-day) variability. *Int J Climatol*, **17**, 1513-1534.

- Flatau, M., P. J. Flatau, P. Phoebus, and P. P. Niiler, 1997: The feedback between equatorial convection and local radiative and evaporative processes: The implications for intraseasonal oscillations. *J Atmos Sci*, **54**, 2373-2386.
- Graham, N. E. and T. P. Barnett, 1987: Sea surface temperature, surface wind divergence and convection over tropical oceans. *Science*, **238**, 657-659.
- Gutzler, D. S., 1991: Interannual Fluctuations of Intraseasonal Variance of near-Equatorial Zonal Winds. *J Geophys Res-Oceans*, **96**, 3173-3185.
- Hayashi, Y. and D. G. Golder, 1993: Tropical 40-50-Day and 25-30-Day Oscillations Appearing in Realistic and Idealized GFDL Climate Models and the ECMWF Dataset. *J Atmos Sci*, **50**, 464-494.
- Hendon, H. H., C. D. Zhang, and J. D. Glick, 1999: Interannual variation of the Madden-Julian oscillation during austral summer. *J Climate*, **12**, 2538-2550.
- Hendon, H. H., B. Liebmann, M. Newman, J. D. Glick, and J. E. Schemm, 2000: Medium-Range Forecast Errors Associated with Active Episodes of the Madden-Julian Oscillation. *Mon Weather Rev*, **128**, 69-86.
- Higgins, R. W. and K. C. Mo, 1997: Persistent North Pacific circulation anomalies and the tropical intraseasonal oscillation. *J Climate*, **10**, 223-244.
- Jones, C., D. E. Waliser, J. K. E. Schemm, and W. K. M. Lau, 2000: Prediction skill of the Madden and Julian Oscillation in dynamical extended range forecasts. *Clim Dynam*, **16**, 273-289.
- Kanamitsu, M., et al., 2002: NCEP dynamical seasonal forecast system 2000. *Bulletin of the American Meteorological Society*, **83**, 1019-1037.

- Krishnamurti, T. N., D. K. Oosterhof, and A. V. Mehta, 1988: Air Sea Interaction on the Time Scale of 30 to 50 Days. *J Atmos Sci*, **45**, 1304-1322.
- Kuma, K., 1994: The Madden and Julian Oscillation and Tropical Disturbances in an Aqua-Planet Version of JMA Global Model With T63 and T159 Resolution. *J Meteorol Soc Japan*, **72**, 147-172.
- Lau, K. M. and F. C. Chang, 1992: Tropical Intraseasonal Oscillation and Its Prediction by the NMC Operational Model. *J Climate*, **5**, 1365-1378.
- Lorenc, A. C., 1984: The Evolution of Planetary-Scale 200-mb Divergent Flow During the FGGE Year. *Quart J Roy Meteorol Soc*, **110**, 427-441.
- Madden, R. A. and P. R. Julian, 1994: Observations of the 40-50-Day Tropical Oscillation - a Review. *Mon Weather Rev*, **122**, 814-837.
- Maloney, E. D. and J. T. Kiehl, 2002: MJO-related SST variations over the tropical eastern Pacific during Northern Hemisphere summer. *J Climate*, **15**, 675-689.
- Mason, S. J., L. Goddard, N. E. Graham, E. Yulaeva, L. Q. Sun, and P. A. Arkin, 1999: The IRI seasonal climate prediction system and the 1997/98 El Nino event. *Bull Amer Meteorol Soc*, **80**, 1853-1873.
- Reichler, T. and J. O. Roads, 2003a: The role of boundary and initial conditions for dynamical seasonal predictability. *Nonlinear Proc Geophys*, (in press).
- Reichler, T. and J. O. Roads, 2003b: Long range predictability in the tropics. Part I: Monthly averages. *J Climate*, (submitted).
- Roads, J. O., 1988: Lagged average predictions in a predictability experiment. *J Atmos Sci*, **45**, 147-162.

- Roads, J. O., S. C. Chen, and F. Fujioka, 2001: ECPC's weekly to seasonal global forecasts. *Bull Amer Meteorol Soc*, **82**, 639-658.
- Rowell, D. P., C. K. Folland, K. Maskell, and M. N. Ward, 1995: Variability of Summer Rainfall Over Tropical North Africa (1906-92) - Observations and Modelling. *Quart J Roy Meteorol Soc*, **121**, 669-704.
- Schemm, J. E., H. Van den Dool, and S. Saha, 1996: A multi-year DERF experiment at NCEP. *11th Conf Numerical Weather Prediction*, Norfolk, Virginia, 47-49.
- Schubert, S. D. and M. L. Wu, 2001: Predictability of the 1997 and 1998 south Asian summer monsoon low-level winds. *J Climate*, **14**, 3173-3191.
- Slingo, J. M. and R. A. Madden, 1991: Characteristics of the Tropical Intraseasonal Oscillation in the NCAR Community Climate Model. *Quart J Roy Meteorol Soc*, **117**, 1129-1169.
- Slingo, J. M., D. P. Rowell, K. R. Sperber, and E. Nortley, 1999: On the predictability of the interannual behaviour of the Madden-Julian Oscillation and its relationship with El Nino. *Quart J Roy Meteorol Soc*, **125**, 583-609.
- Slingo, J. M., et al., 1996: Intraseasonal Oscillations in 15 Atmospheric General Circulation Models - Results From an AMIP Diagnostic Subproject. *Clim Dynam*, **12**, 325-357.
- Toth, Z. and E. Kalnay, 1993: Ensemble Forecasting at NMC - the Generation of Perturbations. *Bull Amer Meteorol Soc*, **74**, 2317-2330.
- van den Dool, H. M. and S. Saha, 1990: Frequency Dependence in Forecast Skill. *Mon Weather Rev*, **118**, 128-137.

- Waliser, D. E., K. M. Lau, and J. H. Kim, 1999a: The influence of coupled sea surface temperatures on the Madden-Julian oscillation: A model perturbation experiment. *J Atmos Sci*, **56**, 333-358.
- Waliser, D. E., C. Jones, J. K. E. Schemm, and N. E. Graham, 1999b: A statistical extended-range tropical forecast model based on the slow evolution of the Madden-Julian oscillation. *J Climate*, **12**, 1918-1939.
- Weller, R. A. and S. P. Anderson, 1996: Surface meteorology and air-sea fluxes in the western equatorial Pacific warm pool during the TOGA coupled ocean-atmosphere response experiment. *J Climate*, **9**, 1959-1990.
- Winkler, C. R., M. Newman, and P. D. Sardeshmukh, 2001: A linear model of wintertime low-frequency variability. Part I: Formulation and forecast skill. *J Climate*, **14**, 4474-4494.
- Wu, M. L. C., A. Schubert, I. S. Kang, and D. Waliser, 2002: Forced and free intraseasonal variability over the South Asian monsoon region simulated by 10 AGCMs. *J Climate*, **15**, 2862-2880.
- Zhang, C. D., 1996: Atmospheric Intraseasonal Variability at the Surface in the Tropical Western Pacific Ocean. *J Atmos Sci*, **53**, 739-758.



## Table and Figure Captions

Table 1: Boundary and initial conditions, ensemble size and simulation period for each experiment and the two base runs. ‘r-2’ means NCEP/DOE reanalysis-2. Winter refers to Dec. 15th – Mar. 31st of the following year. ‘rndm.’ indicates randomly chosen initial conditions, ‘obs.’ means observational data (reanalysis-1), ‘cont.’ indicates continuous simulations over all years, and ‘clim.’ indicates climatological boundary conditions.

Fig. 1: Total variance (left) and ratio of external to internal variance (right) of filtered  $\chi_{200}$  from individual members. Shown are averages over all years and members, and over days 40-106 of each season. Units of variance are  $10^{12} \text{ m}^4 \text{ s}^{-2}$ .

Fig. 2: Wavenumber-frequency spectra of unfiltered  $\chi_{200}$  from daily fields of individual members for the 1979-2000 period: (a) from NCEP-NCAR reanalysis, (b) from experiment ICBC, and (c) from experiment IC. Units are  $10^{12} \text{ m}^4 \text{ s}^{-2} \text{ day}$ . Contour levels are 50, 100, 200, 300, 400, 500 and 600. Shading indicates values greater than 200.

Fig. 3: Composite MJO events in Hovmöller representation, derived from filtered  $\chi_{200}$ . Composites were calculated by averaging over  $n$  strongest events based on the value of  $\chi_{200}$  at  $150^\circ\text{E}$ .  $n$  was taken 20 for reanalysis, 200 for ICBC, and 100 for IC. Units are  $10^6 \text{ m}^2 \text{ s}^{-1}$ . Contour levels are from  $-9$  to  $9$  in steps of 2. Negative values are dashed, and positive values are contoured continuously.

Fig. 4: Predictability as function of lead time as measured by the spatial anomaly correlation of filtered  $\chi_{200}$ : (a) are averages over all years, and (b) are averages over neutral-to-weak ENSO years only. Vertical axis denotes correlation (AC).

Fig. 5: (a) As Fig. 4 but for experiment ICBC-r and IC-r verified against reanalysis. The skill from ICBC is shown as reference. (b) Predictability of filtered zonal wind at 200 hPa for experiment ICBC-r verified against reanalysis, and ICBC verified against itself.

Fig. 6: Predictability during individual years as measured by the spatial anomaly correlation (calculated as Fig. 4), averaged over forecast day 0-40 (a) and 41-106 (b). Ordinate denotes AC, and abscissa denotes year of the January of the forecast.

Fig. 7: Annual MJO activity as measured by the spatio-temporal variance of filtered  $\chi_{200}$  from experiment ICBC. Variance was calculated in space along the equator and in time from forecast day 0-40 (a) and 41-106 (b). Ordinate denotes variance in  $10^{12} \text{ m}^4 \text{ s}^{-2}$ . In the top left corner, correlation between activity and predictability from Fig. 6 is shown.

Fig. 8: MJO evolution during northern winter 1992 as measured by the magnitude and sine of the phase of wavenumber-one filtered  $\chi_{200}$ . Thin lines denote individual ensemble members (20 for ICBC, else 10), and thick lines show ensemble mean. Magnitudes indicate anomalies from climatology with units  $10^6 \text{ m}^2 \text{ s}^{-1}$ .

Fig. 9: Trajectory of the MJO in phase space. Shown is the evolution of the complex wavenumber-one coefficient of filtered  $\chi_{200}$  during northern winter 1992 (a) and 1996 (b) for different experiments. Distance from the center denotes magnitude in  $10^6 \text{ m}^2 \text{ s}^{-1}$  (see ICP). Angle from the positive x-axis represents phase. Time is shown in colors and by numbers for ICBC (1992). It changes every 5 days, starting with red (day 0-4), and ending with purple (day 105-107). The geographical locations mark the approximate center of maximum convection for a given phase angle.

Fig. 10: Predictability of magnitude (a) and phase (b) of wavenumber one filtered  $\chi_{200}$  as function of lead time, and as measured by the temporal correlations. The curves are smoothed with a 21 days moving average filter. Vertical axis denotes correlation.

Fig. 11: Variability of tropical SSTs during northern winter at 54 days period, summed over eastward traveling wavenumbers 0-3. Units are  $K^2$  day.

Fig. 12: Unfiltered SST anomalies during 1992 in time-longitude representation. Units are in  $^{\circ}K$ . Black contours show filtered  $\chi_{200}$  from reanalysis (a) and ICBC (b).

Fig. 13: Composite MJO events (contours) and associated SST anomalies (shading) for simulation ICBC (top panels) and reanalysis (bottom panels). Shown are composites of 200 (ICBC) or 10 (reanalysis) strongest MJO events, as given by negative anomalies of filtered  $\chi_{200}$  at the base point ( $90^{\circ}E$  left panel,  $150^{\circ}E$  right panel). Contour interval is from  $-6 \cdot 10^6 \text{ m}^2\text{s}^{-1}$  in intervals of 2. Negative values are dashed. SST anomalies are standardized by the local interannual standard deviation.

Fig. 14: Temporal correlation between composite MJO and SST (as shown in Fig. 13) for base points at  $90^{\circ}E$  (a) and  $150^{\circ}E$  (b). Ordinate denotes temporal correlation, and abscissa denotes west- or eastward shift of SSTs.

## Table and Figures

Table 1: Boundary and initial conditions, ensemble size and simulation period for each experiment and the two base runs. ‘r-2’ means NCEP/DOE reanalysis-2. Winter refers to Dec. 15th – Mar. 31st of the following year. ‘rndm.’ indicates randomly chosen initial conditions, ‘obs.’ means observational data (reanalysis-1), ‘cont.’ indicates continuous simulations over all years, and ‘clim.’ indicates climatological boundary conditions.

<i>name</i>	<i>boundary conditions</i>		<i>initial conditions</i>		<i>size</i>	<i>period</i>	<i>years</i>
	<i>ocean</i>	<i>land</i>	<i>atmosphere</i>	<i>land</i>			
BASE-O	observed	model	obs. 1/1/48	obs. 1/1/48	1	cont.	1948-2000
BASE-C	clim.	model	obs. 1/1/48	obs. 1/1/48	1	cont.	1948-2024
ICBC	observed	model	BASE-O	BASE-O	20	winter	1979-2000
ICBC-r	observed	r-2	r-2	-	10	winter	1979-2000
ICP	persisted	model	BASE-O	BASE-O	10	winter	1979-2000
IC	clim.	r-2 clim.	BASE-O	-	10	winter	1979-2000
IC-r	clim.	r-2 clim.	r-2	-	10	winter	1979-2000
BC	observed	model	BASE-C rndm.	BASE-C rndm.	10	winter	1979-2000
iBC	observed	model	ICBC, 1 yr lag	ICBC, 1 yr lag	10	winter	1980-2001

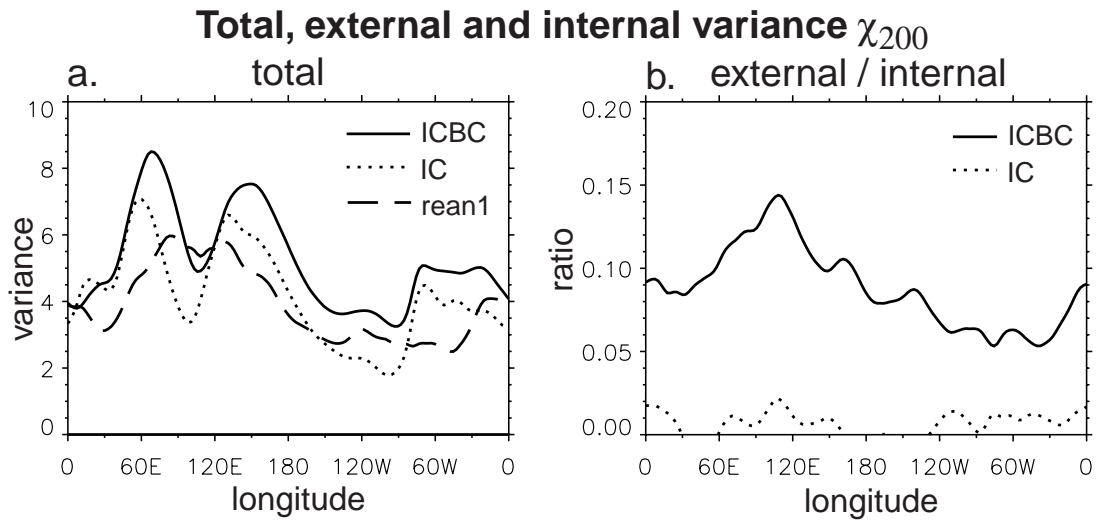


Fig. 1: Total variance (left) and ratio of external to internal variance (right) of filtered  $\chi_{200}$  from individual members. Shown are averages over all years and members, and over days 40-106 of each season. Units of variance are  $10^{12} \text{ m}^4 \text{ s}^{-2}$ .

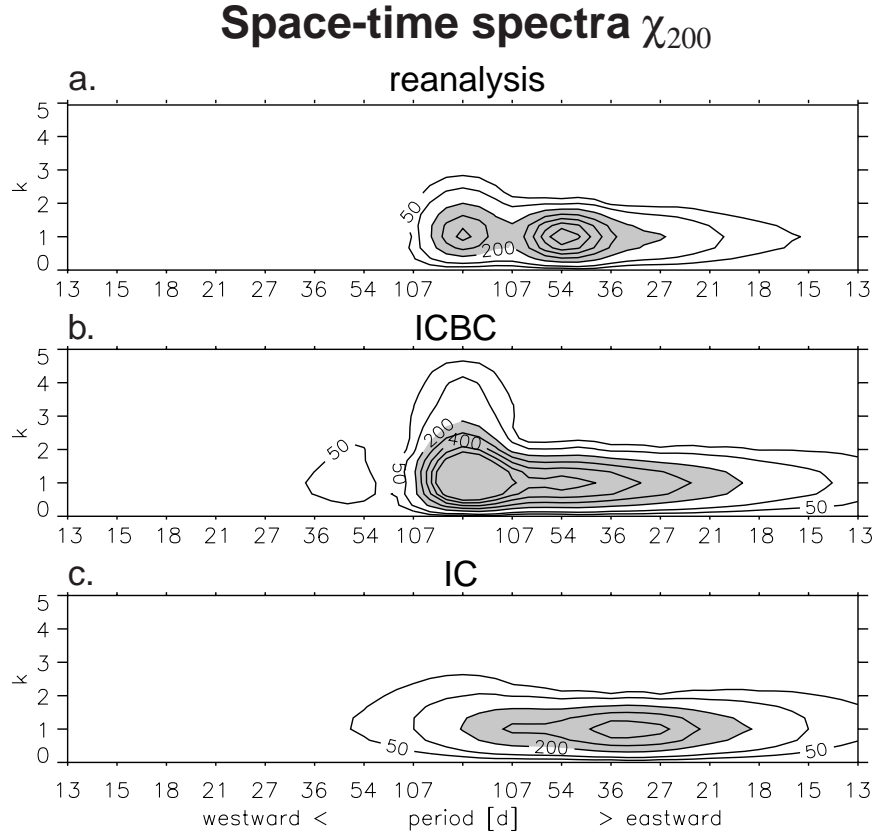


Fig. 2: Wavenumber-frequency spectra of unfiltered  $\chi_{200}$  from daily fields of individual members for the 1979-2000 period: (a) from NCEP-NCAR reanalysis, (b) from experiment ICBC, and (c) from experiment IC. Units are  $10^{12} \text{ m}^4 \text{ s}^{-2} \text{ day}$ . Contour levels are 50, 100, 200, 300, 400, 500 and 600. Shading indicates values greater than 200.

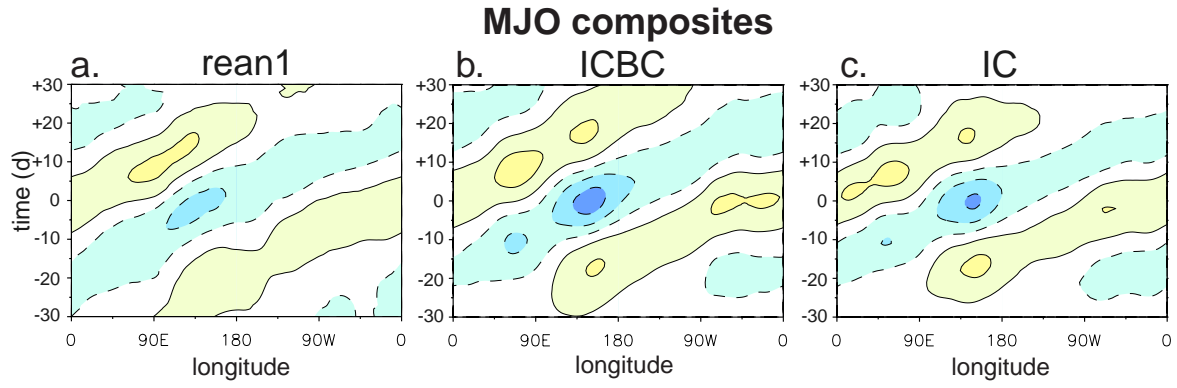


Fig. 3: Composite MJO events in Hovmöller representation, derived from filtered  $\chi_{200}$ . Composites were calculated by averaging over  $n$  strongest events based on the value of  $\chi_{200}$  at  $150^\circ\text{E}$ .  $n$  was taken 20 for reanalysis, 200 for ICBC, and 100 for IC. Units are  $10^6 \text{ m}^2\text{s}^{-1}$ . Contour levels are from  $-9$  to  $9$  in steps of 2. Negative values are dashed, and positive values are contoured continuously.

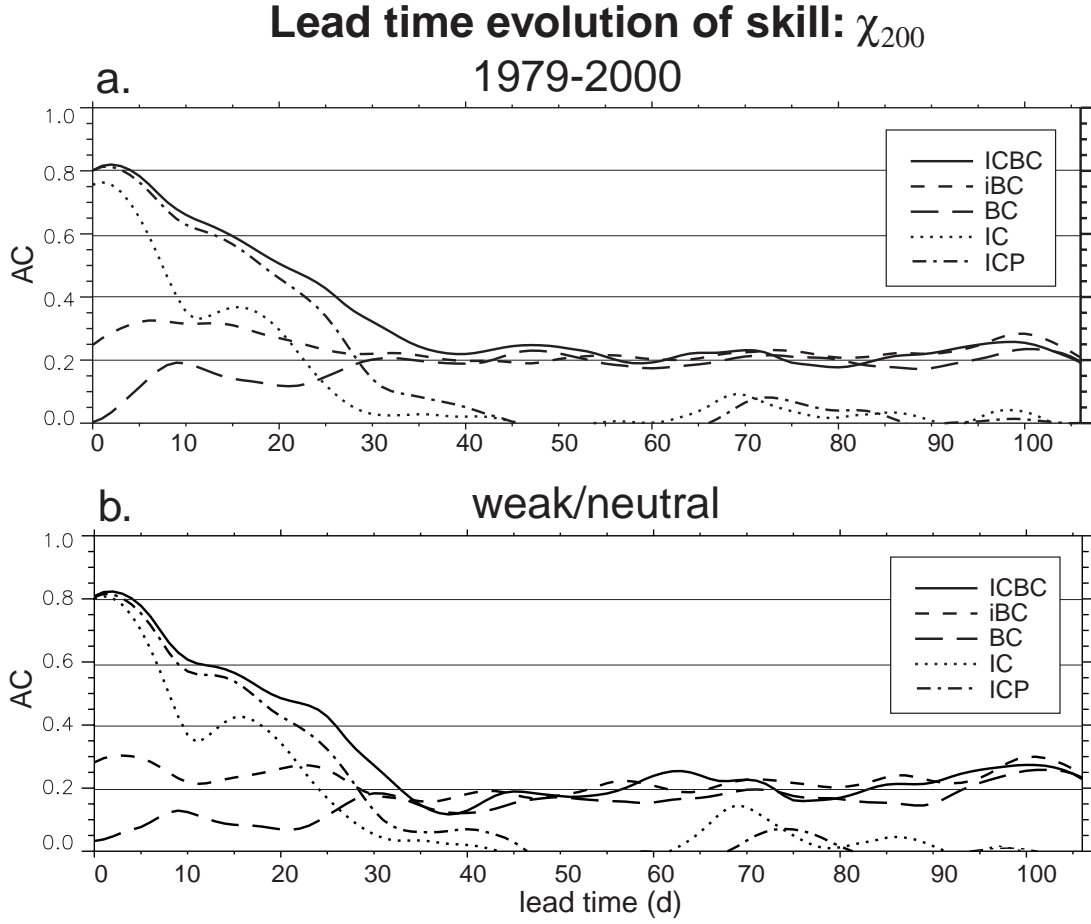


Fig. 4: Predictability as function of lead time as measured by the spatial anomaly correlation of filtered  $\chi_{200}$ : (a) are averages over all years, and (b) are averages over neutral-to-weak ENSO years only. Vertical axis denotes correlation (AC).



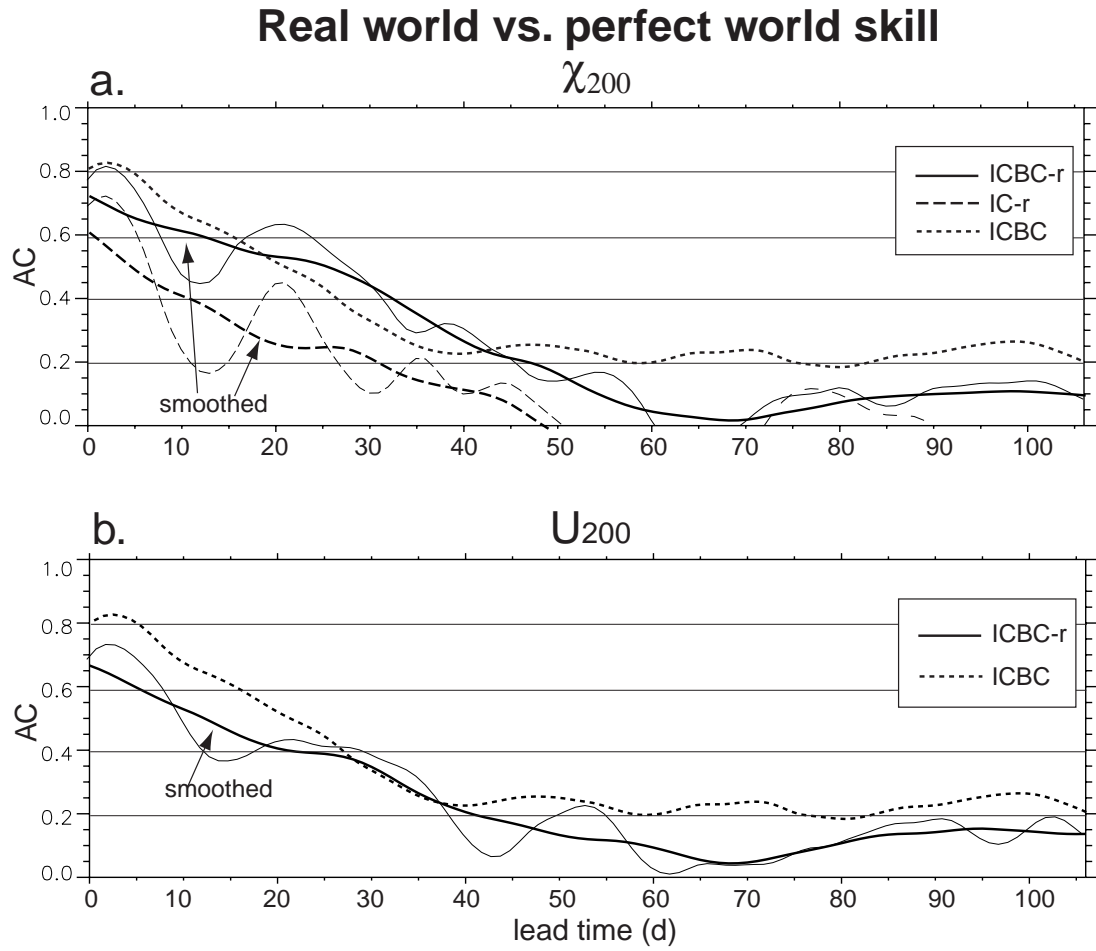


Fig. 5: (a) As Fig. 4 but for experiment ICBC-r and IC-r verified against reanalysis. The skill from ICBC is shown as reference. (b) Predictability of filtered zonal wind at 200 hPa for experiment ICBC-r verified against reanalysis, and ICBC verified against itself.

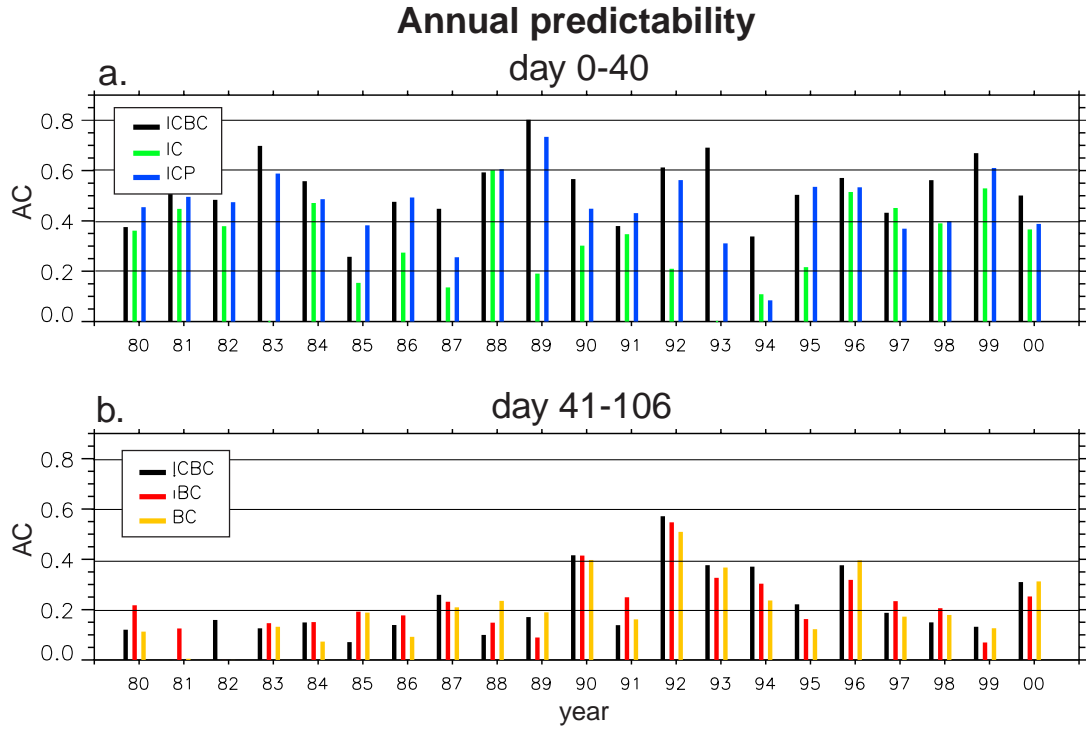


Fig. 6: Predictability during individual years as measured by the spatial anomaly correlation (calculated as Fig. 4), averaged over forecast day 0-40 (a) and 41-106 (b). Ordinate denotes AC, and abscissa denotes year of the January of the forecast.

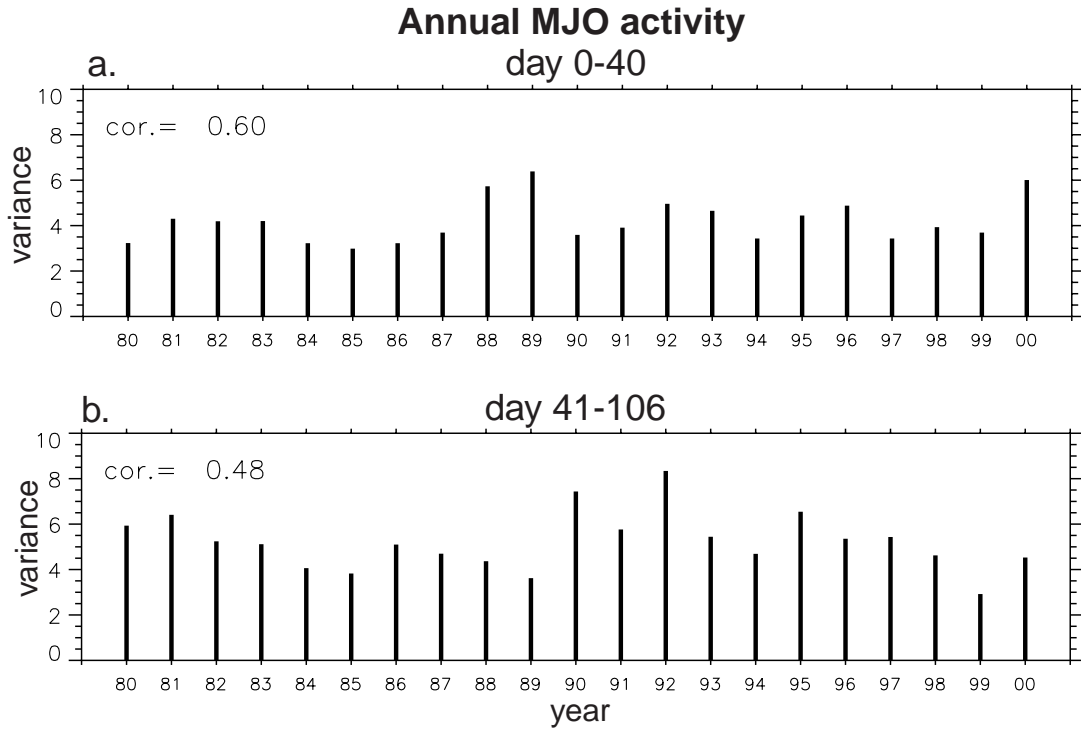


Fig. 7: Annual MJO activity as measured by the spatio-temporal variance of filtered  $\chi_{200}$  from experiment ICBC. Variance was calculated in space along the equator and in time from forecast day 0-40 (a) and 41-106 (b). Ordinate denotes variance in  $10^{12} \text{ m}^4 \text{ s}^{-2}$ . In the top left corner, correlation between activity and predictability from Fig. 6 is shown.

## MJO during northern winter 1992

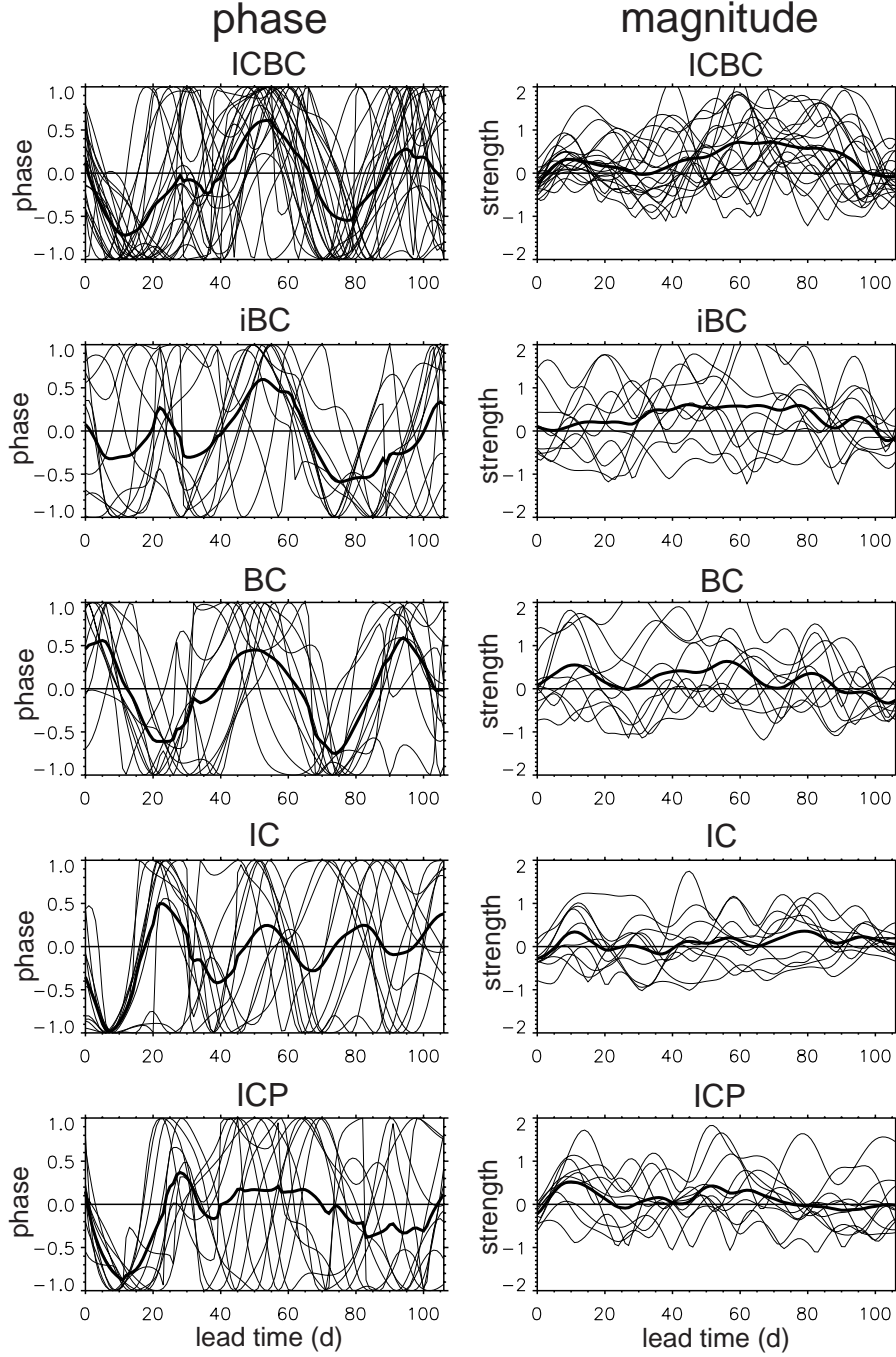


Fig. 8: MJO evolution during northern winter 1992 as measured by the magnitude and sine of the phase of wavenumber-one filtered  $\chi_{200}$ . Thin lines denote individual ensemble members (20 for ICBC, else 10), and thick lines show ensemble mean. Magnitudes indicate anomalies from climatology with units  $10^6 \text{ m}^2 \text{ s}^{-1}$ .

## MJO in phase space representation

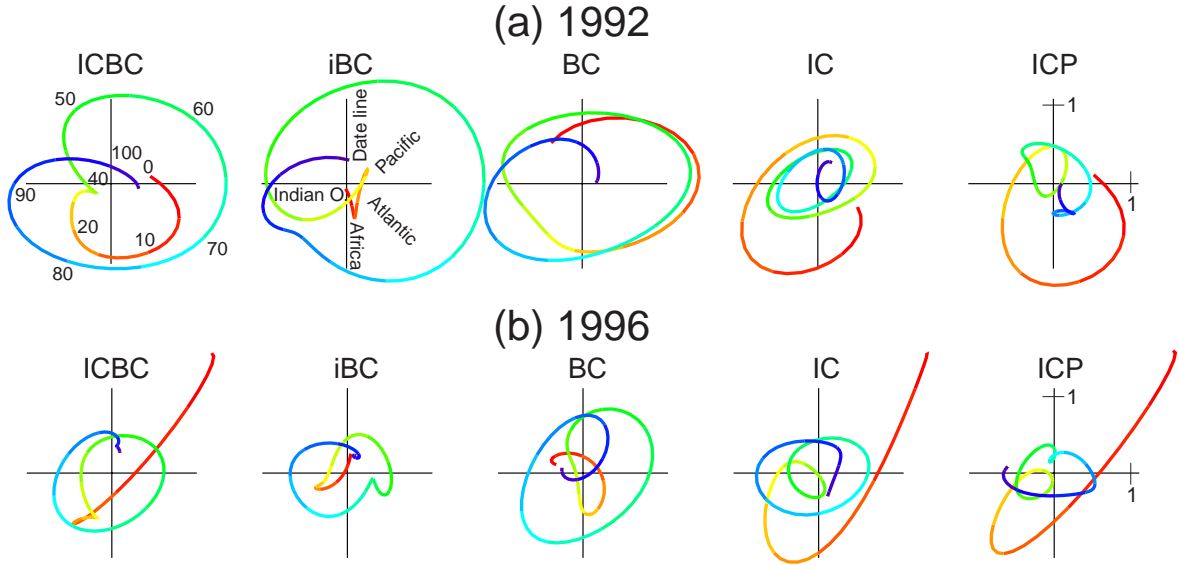


Fig. 9: Trajectory of the MJO in phase space. Shown is the evolution of the complex wavenumber-one coefficient of filtered  $\chi_{200}$  during northern winter 1992 (a) and 1996 (b) for different experiments. Distance from the center denotes magnitude in  $10^6 \text{ m}^2 \text{ s}^{-1}$  (see ICP). Angle from the positive x-axis represents phase. Time is shown in colors and by numbers for ICBC (1992). It changes every 5 days, starting with red (day 0-4), and ending with purple (day 105-107). The geographical locations mark the approximate center of maximum convection for a given phase angle.

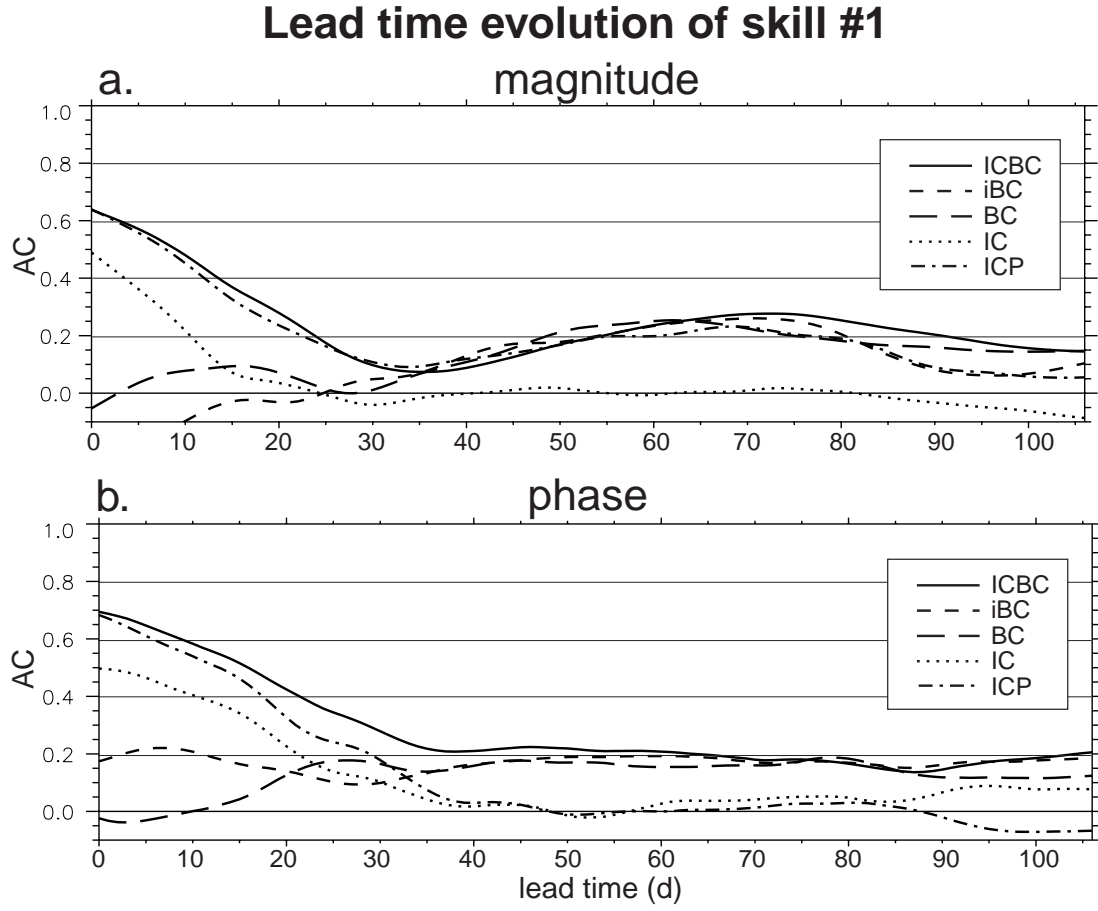


Fig. 10: Predictability of magnitude (a) and phase (b) of wavenumber one filtered  $\chi_{200}$  as function of lead time, and as measured by the temporal correlations. The curves are smoothed with a 21 days moving average filter. Vertical axis denotes correlation.

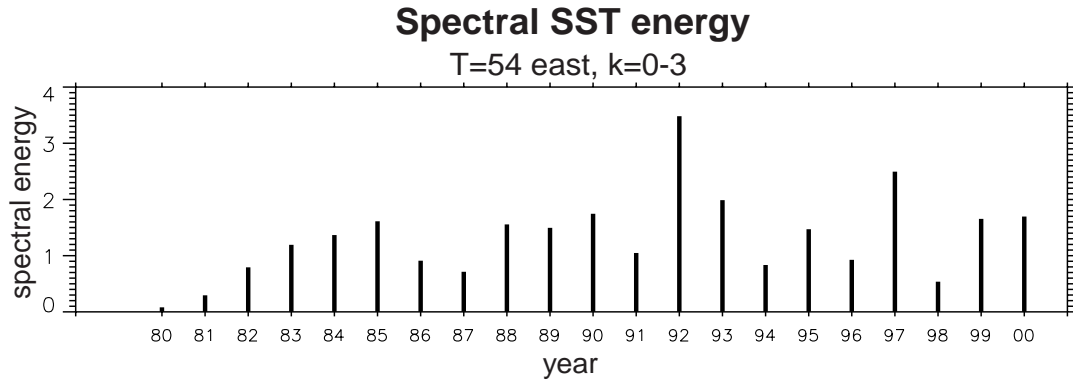


Fig. 11: Variability of tropical SSTs during northern winter at 54 days period, summed over eastward traveling wavenumbers 0-3. Units are  $K^2 \text{ day}$ .

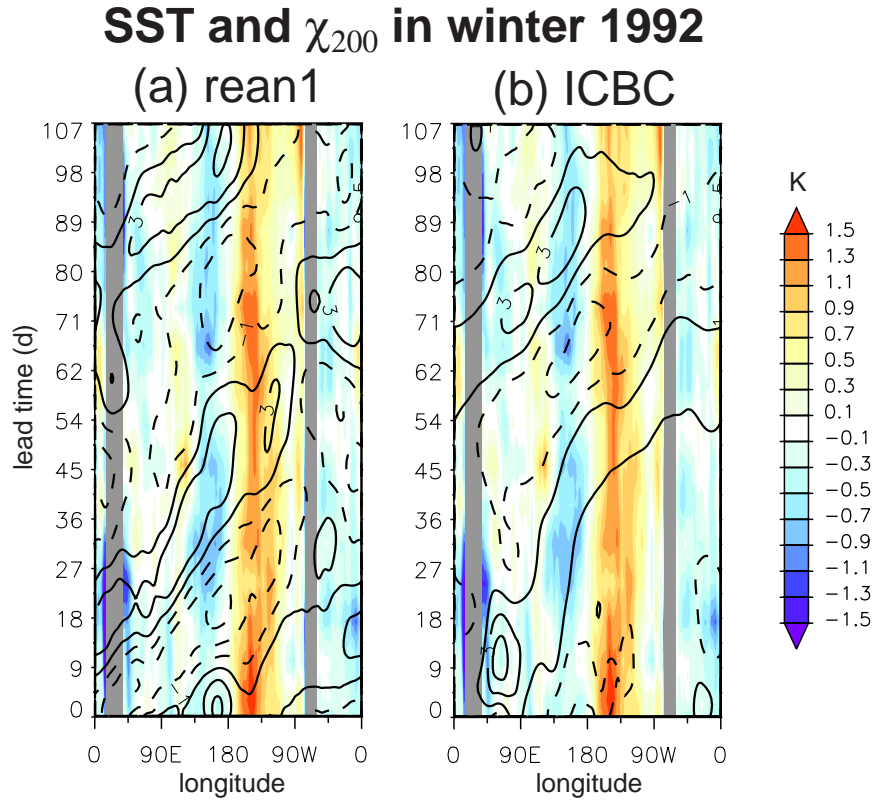


Fig. 12: Unfiltered SST anomalies during 1992 in time-longitude representation. Units are in  $^{\circ}K$ . Black contours show filtered  $\chi_{200}$  from reanalysis (a) and ICBC (b).

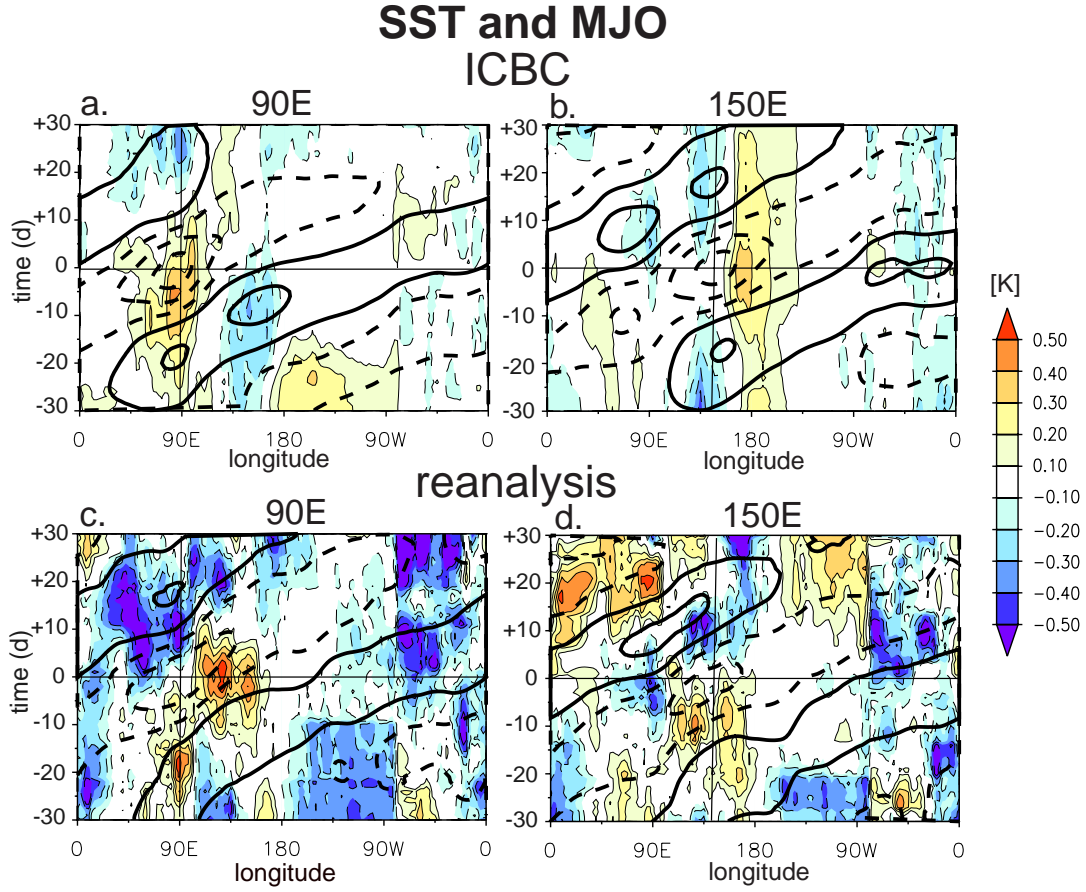


Fig. 13: Composite MJO events (contours) and associated SST anomalies (shading) for simulation ICBC (top panels) and reanalysis (bottom panels). Shown are composites of 200 (ICBC) or 10 (reanalysis) strongest MJO events, as given by negative anomalies of filtered  $\chi_{200}$  at the base point (90°E left panel, 150°E right panel). Contour interval is from  $-6 \cdot 10^6 \text{ m}^2 \text{ s}^{-1}$  in intervals of 2. Negative values are dashed. SST anomalies are standardized by the local interannual standard deviation.



## Correlation between MJO and SST

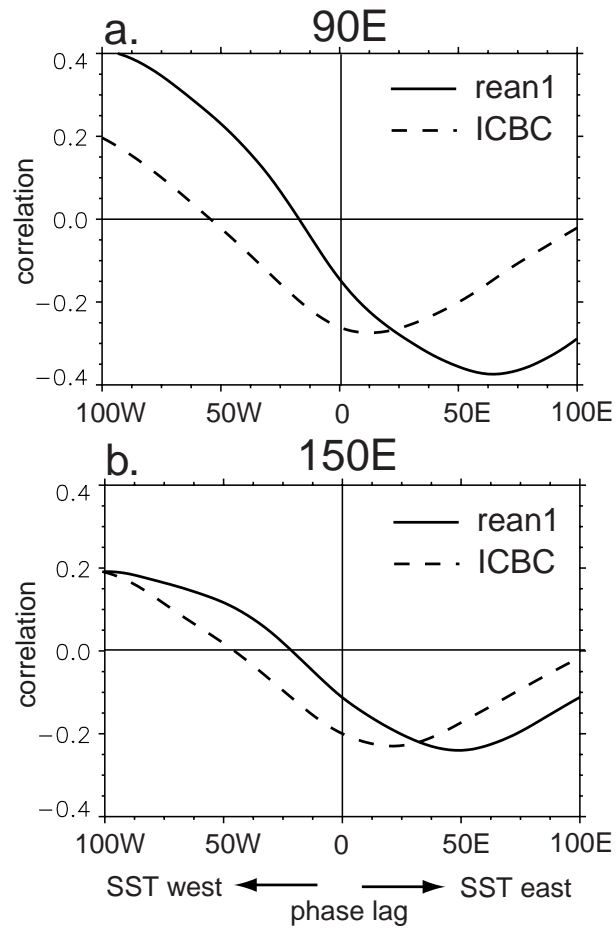


Fig. 14: Temporal correlation between composite MJO and SST (as shown in Fig. 13) for base points at 90°E (a) and 150°E (b). Ordinate denotes temporal correlation, and abscissa denotes west- or eastward shift of SSTs.